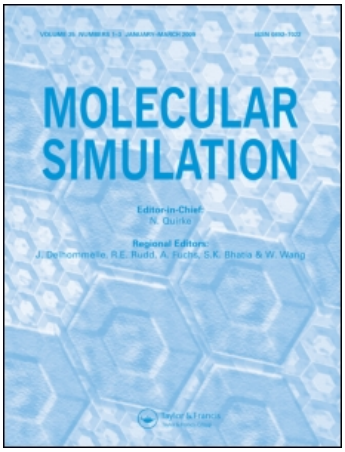

Molecular Simulation
Publication details, including instructions for authors and subscription information:
http://www.informaworld.com/smpp/title~content=t713644482

Molecular simulation applied to fluid properties in the oil and gas industry

P. Ungerer[a]; C. Nieto-Draghi[a]; V. Lachet[a]; A. Wender[b]; A. di Lella[b]; A. Boutin[b]; B. Rousseau[b]; A. H. Fuchs[c]
[a] Institut Français du Pétrole, Rueil-Malmaison, France [b] Laboratoire de Chimie Physique, Université de Paris Sud—CNRS, Orsay, France [c] Ecole Nationale Supérieure de Chimie de Paris (ENSCP), Paris Cedex 05, France

To cite this Article Ungerer, P. , Nieto-Draghi, C. , Lachet, V. , Wender, A. , di Lella, A. , Boutin, A. , Rousseau, B. and Fuchs, A. H.(2007) 'Molecular simulation applied to fluid properties in the oil and gas industry', Molecular Simulation, 33: 4, 287 — 304
To link to this Article: DOI: 10.1080/08927020701245509
URL: http://dx.doi.org/10.1080/08927020701245509

Molecular Simulation, Vol. 33, Nos. 4–5, 15–30 April 2007, 287–304

Taylor & Francis
Taylor & Francis Group

Molecular simulation applied to fluid properties in the oil and gas industry

P. UNGERER†*, C. NIETO-DRAGHI†, V. LACHET†, A. WENDER†‡, A. DI LELLA†‡, A. BOUTIN‡, B. ROUSSEAU‡ and A. H. FUCHS‡¶

†Institut Français du Pétrole, 1–4 avenue de Bois Préau, 92852 Rueil-Malmaison, France
‡Laboratoire de Chimie Physique, Université de Paris Sud—CNRS, 91405 Orsay, France
¶Ecole Nationale Supérieure de Chimie de Paris (ENSCP), 11 rue Pierre et Marie Curie, 75231 Paris Cedex 05, France

(Received June 2006; in final form January 2007)

In order to illustrate the use of molecular simulation methods in the oil and gas industry, three typical fields of application are considered. The first of these is the prediction of fluid phase equilibria by Gibbs ensemble simulation, exemplified here by the systematic determination of full phase diagrams (including liquid–vapour critical points) for binary systems of hydrogen sulphide and various hydrocarbons (*n*-alkanes with 2–20 carbon atoms, benzene, ethylbenzene, cyclohexane). The second type of application is the adsorption equilibria in zeolites. For these applications, the comprehensive modelling of the interplay of hydrocarbon adsorption with polar compounds (alkanethiols, water) and cation mobility is a still a challenge for simulation methods. However encouraging results are shown when the different contributions to interaction energy (dispersion–repulsion, electrostatic, polarization) are separately addressed when simulating the adsorption of *n*-alkanes in sodium faujasites. The third field considered is the determination of transport properties, particularly viscosity, from equilibrium molecular dynamics (MD). Although they describe rather well the influence of pressure, temperature and carbon number, existing force fields for *n*-alkanes are found to underestimate the viscosity of liquids. By a specific modification of the torsion potential which does not alter the equilibrium conformations, the viscosity is significantly improved without compromising phase equilibrium properties. A brief outline of other current and future applications of molecular simulation in the oil and gas industry is given in conclusion.

Keywords: Molecular simulation; Gibbs ensemble simulation; Phase equilibrium; Phase diagrams; Molecular dynamics; Viscosity; Adsorption; Zeolites

1. Introduction

The oil and gas industry shares with the chemical industry the need for fluid property predictions over a large domain of conditions. The fluids to be considered are not only composed of hydrocarbons, as interactions with water and acid gases (carbon dioxide, hydrogen sulfide) are important in reservoir engineering and many sulfur-bearing or oxygen-bearing organic compounds are present, either as impurities to be removed, or as solvents at various stages of hydrocarbon production and processing. Pressure may be as high as 120 MPa in deep reservoirs and 200 MPa in the injection devices of fuel in recent diesel engines. Temperature conditions range from the conditions of liquefied natural gas (110 K) to those of hydrocracking (700 K). This industry has been thus a privileged user of thermodynamic data [1,2], concepts and models developed since the beginning of the 20th century. Among the various models that are intensively used today to predict the equilibrium properties of pure fluids and mixtures, we can quote equations of state [3–7], group contribution methods [8] and excess Gibbs energy models [9–11]. Physisorption in microporous adsorbents, which is the basis of important separation processes, can be modelled using several types of classical or less classical models [12,13]. The viscosity of fluids can be modelled by adapted gas viscosity models [14], corresponding states methods [15], group contributions [16] or correlations [17]. More complete references can be found in reference textbooks [18–20].

Although the above quoted methods are sufficient in many cases, they suffer from significant drawbacks when experimental data are lacking for parametrization or validation. Beyond 10 carbon atoms, numerous pure

*Corresponding author. Email: philippe.ungerer@ifp.fr

Molecular Simulation
ISSN 0892-7022 print/ISSN 1029-0435 online © 2007 Taylor & Francis
http://www.tandf.co.uk/journals
DOI: 10.1080/08927020701245509

hydrocarbons that can be identified by conventional analysis methods are not commercially available at a reasonable price, so that their thermodynamic and transport properties have never been measured. These properties are obtained by group contribution methods, but their reliability is uncertain and in most cases, these methods cannot differentiate among isomers. In the case of mixtures, phase equilibrium predictions are often hampered by the lack of experimental data when toxic or unstable compounds are involved, or when extreme pressure and temperature conditions are considered. In the case of transport properties, the frequent lack of experimental data and the lower extrapolation capability of classical models makes predictions often uncomfortable. When adsorption in microporous solids like zeolites is considered, great difficulties are encountered to predict the influence of the crystalline structure and molecular structure on the adsorption properties of pure compounds and more importantly, of mixtures. Predicting adsorption selectivity is probably one of the most difficult challenges of applied thermodynamics for our industry.

In order to solve these persisting difficulties, molecular simulation presents the advantage of sound theoretical framework, in which the knowledge of interactions at the molecular scale allows to address fluid phase equilibria, adsorption in microporous solids and transport properties. It is the aim of the present study to illustrate how this technology is now used in the oil and gas industry, on the basis of three specific industrial applications. It is thus not aimed at providing a comprehensive account of available simulation methods and achievements, for which detailed reviews are available [21–24].

The first of these projects is related to the investigation of the phase behavior of mixtures involving hydrogen sulphide and liquid hydrocarbons. Its motivation is mainly the production of H_2S-rich oils or gases, which could be made more economic by reinjecting hydrogen sulfide in deep reservoirs after it has been separated from the produced fluid. The results presented here are the continuation of previous work in which the mixtures of H_2S with propane [25], *n*-pentane [26], methanol [23], methane and water [27] were investigated. In the present study, the evaluation of simulation methods and the consideration of heavier hydrocarbons will take a prominent place. We will thus compare two sampling methods, the Gibbs ensemble [28] and Gibbs–Duhem integration [29]. We will also compare different force fields for aromatics and the determination of liquid–vapour critical points will be treated in detail.

The second type of project that will be considered in this article is the simulation of adsorption in zeolites. Molecular simulation has allowed to address linear and branched alkane adsorption for a significant range of zeolites [30–40]. Meanwhile, our group has investigated the adsorption of aromatics in faujasites, a delicate problem in which the location of cations and the electrostatic interactions play a major role [23,41,42]. Monte Carlo simulation has also provided encouraging answers to the location of cations, which is not always available from experimental measurements and may be influenced by the presence of water in laboratory measurements or in industrial processes [43–45]. In the present article, we will illustrate the role of the different energy contributions (dispersion–repulsion, electrostatic, polarization) by recent simulation results involving mainly the adsorption of alkanes, alkanethiols, water and their mixtures.

Finally, the third application considered in this work will be the investigation of viscosity of hydrocarbons at high pressure, using molecular dynamics (MD). Here, the motivation is mainly the understanding of viscosity of fuels in the high pressure conditions encountered in the injection line of engines (up to 200 MPa). The need to predict viscosity in reservoir conditions (up to 120 MPa) or in hydrocarbon processing (up to 700 K) is an additional reason for investigating extreme conditions. For such applications, the difficulty of performing viscosity measurements is not only due to the cost of high pressure equipment or to the rapid thermal degradation of hydrocarbons above 650 K, but also to the unavailability of pure compounds. Thanks to the implementation of adapted algorithms to simulate various ensembles [46–48] and to handle flexible alkanes [49,50], equilibrium MD has been applied to the prediction of viscosity for linear and branched alkanes [51–57], cyclohexane [57] and aromatics [57,58], with encouraging results. However, these predictions have not yet covered a sufficient range of temperatures, pressures and carbon numbers. In the present work, we will investigate mainly the viscosity of *n*-alkanes and discuss how intermolecular potentials should be improved to provide useful predictions for industrial applications.

2. Fluid phase equilibria of H_2S–hydrocarbon systems

2.1 Simulation methods and conditions

2.1.1 Gibbs ensemble. Phase equlibrium is simulated with the Gibbs ensemble technique [28] in which two simulation boxes without explicit interfaces represent the vapour and liquid phases. In contrast to pure component calculations, which use the Gibbs ensemble at imposed global volume, binary and multicomponent mixtures are more often simulated at constant pressure. Five types of Monte Carlo moves are used to sample the internal configurations of a given box: rigid body translation and rigid body rotation of a molecule, regrowth of part of an alkyl chain by configurational bias [59], flip, i.e. rotation of a force centre around the axis formed by its immediate neighbours in linear alkyl chains or cyclic alkanes and reptation, i.e. deletion of force centers at one end and regrowth at the other end of the chain. Volume changes are used to satisfy mechanical equilibrium at the desired pressure and molecule transfers between phases are used to impose equal chemical potentials in both simulation

boxes. The latter moves are based on configurational bias for *n*-alkanes [59] or on the reservoir bias [34,60,61] for cyclic alkanes and rigid molecules. Both algorithms are used simultaneously for mixed rigid–flexible molecules such as alkylbenzenes.

The configurational bias algorithm consists in growing the molecule centre by centre, testing several possible locations for each new centre. This algorithm is well adapted to linear flexible molecules. It has been used here for *n*-alkanes and for alkyl substituents of benzenic rings.

The flip [62] is a move of a single group to relax the internal part of a linear chain more simply than the concerted rotation algorithm [63]. Although less efficient than the latter for very long chains, it is sufficient to relax the *n*-alkanes, alkyl chains and cyclic alkanes considered in the present study. The reptation has been applied only to linear molecules, such as *n*-alkanes in our study.

In our implementation, the reservoir bias algorithm [61] involves two steps. The first step involves the selection of a suitable location for inserting a new molecule by testing several places with a simple Lennard–Jones particle. The second step involves testing of several molecular orientations and conformations (selected randomly in a suitable reservoir of conformations) with the centre of mass at the location selected in the first step. This algorithm has been used not only for cyclic flexible molecules, for which it is particularly well adapted, but also for rigid molecules like benzene, H_2S, or CO_2. The decomposition of the move in two steps makes it indeed particularly efficient.

2.1.2 Gibbs–Duhem integration and grand canonical ensemble. Gibbs–Duhem integration [29] is a way to compute phase diagrams of binary systems without using the Gibbs ensemble. The general principle is that one point of the diagram must be known from either experiments or from an alternative phase equilibrium calculation method (Gibbs ensemble Monte Carlo for instance). Then, a suitable form of the Gibbs–Duhem equation is used in an iterative process to obtain successive coexistence points:

$$v\,\mathrm{d}P = \sum_i N_i \mathrm{d}\mu_i \tag{1}$$

where v is phase volume, P is pressure, N_i and μ_i are the number of molecules and the chemical potential of species i. In this stepwise integration process, advantage is taken that monophasic simulations of both phases allow to determine the derivatives of the chemical potential of each species.

In its original version, the Gibbs–Duhem integration involves molecular simulations in a specific ensemble in which the fugacity ratio of both components is imposed [29]. Here we have devised a modified version of the Gibbs–Duhem algorithm that can be operated on the basis of grand canonical simulations only, which are more routinely available. This method involves the following steps.

In a first step, a Gibbs ensemble calculation at imposed pressure P^0 is used to provide the starting point. The collected results for the method are the average number of molecules of each component in the vapour phase

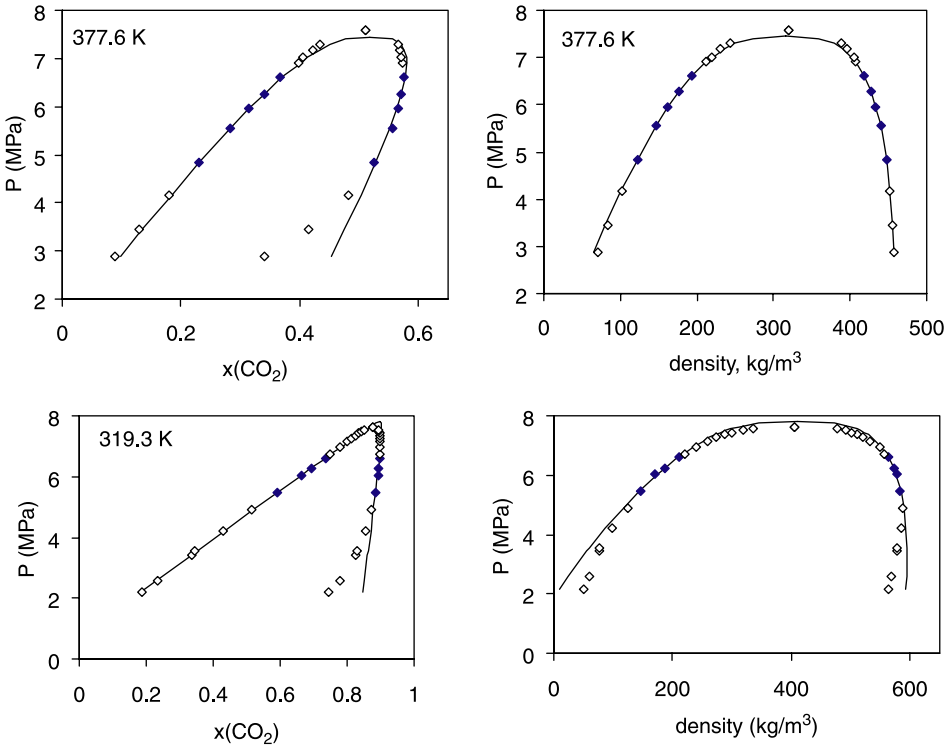

Figure 1. Liquid–vapour coexistence curves of the butane–carbon dioxide system at 377.6 and 319.3 K in the pressure–composition diagram (left) and pressure–density diagram (right). Experimental data [66] are indicated by symbols. The regressed scaling laws equations (8) and (9) are indicated by solid lines. The reference data points for the regression are shown as filled symbols (reprinted from Ref. [23]).

$(N_1^{V,0}, N_2^{V,0})$ and in the liquid phase $(N_1^{L,0}, N_2^{L,0})$, the phase volumes (v^V, v^L) and chemical potentials (μ_1^0, μ_2^0).

In a second step, the Gibbs–Duhem equation is written to determine what should be the chemical potentials μ_1^1, μ_2^1 of the components in equilibrium conditions at a different pressure level P_1. This step does not involve any molecular simulation, but a simple spreadsheet calculation.

In a third step, two grand canonical simulations are conducted. Both simulations use the same chemical potentials (μ_1^1, μ_2^1) but they differ in their initial density. The simulation of the grand canonical ensemble, which is used to implement the Gibbs–Duhem integration technique, involves the same internal moves as the Gibbs ensemble (translations, rotations, regrowth, flips). In addition to these moves, it requires insertions of a new molecule and deletion of an existing molecule. The average number of molecules in each phase is collected in these simulations and the average pressure is then determined for each phase from the virial equation. It has to be checked first that phase pressures are equal to the target pressure P^1 within statistical uncertainties. In fact, the statistical uncertainty on pressure is much larger in the liquid than in the vapour phase, so that this test is more relevant for the latter.

If the test is successful, the steps 2 and 3 can then be repeated for the next target pressure P^2 and further steps $P^3 \ldots P^n$ can be treated in the same way. If pressures are not found equal to the target pressure, the integration scheme is not accurate enough and the likely cause is an excessive spacing between P^n and P^{n+1}. Then the step must be performed again with a lower pressure spacing. This integration scheme is first-order (the chemical potential at step n and its derivative at step n are used to evaluate the chemical potential at step $n + 1$). It would be possible as well to use a second order scheme, in which the chemical potential at step n and its derivative at step n would be used to evaluate the chemical potential at step $n + 1$. This would allow us to use a larger spacing of pressure levels, but the spacing should be regular. It has not been tested however.

In practice, it has been found sufficient to use a pressure spacing of 1 MPa, which was reduced to approximately 0.5 MPa in the upper pressure range because phase concentrations change more rapidly in this part of the diagram which is closer to critical conditions. With higher pressures, it was necessary to increase the box size, otherwise the near-critical fluctuations resulted in poorly representative densities.

2.1.3 Determination of liquid–vapour critical points. In the case of pure components, it is well known that the large characteristic size of the density fluctuations makes it impossible to perform simulations in the close vicinity of the critical point. The determination of the critical temperature T_c and of the critical density ρ_c is nevertheless possible by extrapolation from simulation points sufficiently far away from the critical point, assuming the following scaling law:

$$\rho^V - \rho^L = A(T - T_c)^\beta \tag{2}$$

where $\beta \approx 0.325$ is a characteristic universal exponent [64,65]. It is also assumed that the densities of the coexisting liquid and vapour obey the so-called law of rectilinear diameters:

$$\frac{\rho^V + \rho^L}{2} - \rho_c = B(T - T_c) \tag{3}$$

Practically, T_c and ρ_c are regressed by a least square method minimizing the average deviation between the above equations and the simulated coexistence densities at several temperatures.

When a binary mixture involves a liquid component and a supercritical component, the isothermal (P, x) diagram is often displaying a liquid–vapour critical point which corresponds to the higher pressure of the two-phase envelope. For the same reason as pure compounds, Gibbs ensemble simulations of mixtures cannot be performed close to the critical point. The critical pressure, critical density and critical compositions must be determined by some extrapolation, based on adequate scaling laws. At a given temperature, binary systems are characterized by two coexistence curves in the pressure–density (P, x) diagram and in the pressure–composition (P, ρ) diagram. While the pressure–density coexistence curve of binary mixtures is much alike the temperature–density curve of pure compounds, the pressure–composition coexistence curve may display a quite different shape, depending on the temperature considered. This is illustrated by the butane–carbon dioxide system, for which accurate data are available [66]. At the temperature of 377.6 K, the (P, x) coexistence curve is rather flat near the critical point, while it is much narrower and sharp at 319.3 K ((figure 1)). As proposed in a recent work [23], we use expansion formulae for density and composition that are consistent with near-critical scaling behaviour and flexible enough to reproduce the various possible diagram shapes in the (P, x) curves.

In order to match the pressure–density behaviour, we use the same scaling laws as pure compounds, except that temperature is replaced by pressure:

$$\rho^V - \rho^L = \gamma\,(P - P_c)^\beta \tag{4}$$

$$\frac{\rho^V + \rho^L}{2} - \rho_c = \lambda(P - P_c) \tag{5}$$

In the near-critical region of binary mixtures, the composition difference has been found to behave in the same way as density, i.e. the leading term is of the type $(P - P_c)^\beta$, the critical exponent being unchanged [67,68]. In an investigation of the scaling behavior of Lennard–Jones fluid mixtures by histogram reweighting, Potoff and Panagiotopoulos [69] found as well that the same critical exponents apply to mixtures and pure fluids.

In order to represent the pressure–composition diagram, the near-critical scaling law is complemented with a linear term:

$$x_v - x_l = \lambda_1(P_c - P) + \mu(P_c - P)^\beta \quad (6)$$

Compared with pure components, this may be seen as adding a higher order term in a Taylor-like expansion to match the observed behaviour at some distance from the critical point. In the close vicinity to the critical point, the linear term vanishes compared with the β-exponent term.

An equivalent relationship as equation (5) may be used for the mid-composition:

$$\frac{1}{2}(x_v + x_l) = \lambda_2(P_c - P) \quad (7)$$

The resulting expressions for the coexisting densities and compositions are then given by:

$$\rho_i = \rho_c + \varepsilon\frac{\gamma}{2}(P_c - P)^\beta + \lambda(P_c - P) \quad (8)$$

$$x_\varphi = x_c + \left(\lambda_1 - \varepsilon\frac{\lambda_2}{2}\right)(P_c - P) - \varepsilon\frac{\mu}{2}(P_c - P)^\beta \quad (9)$$

where $\varepsilon = 1$ for the liquid phase and $\varepsilon = -1$ for the vapour phase.

For a given temperature, the regression of the eight parameters $P_c, \gamma, \lambda, \rho_c, \lambda_1, \mu, x_c, \lambda_2$ involved in these expressions (4)–(9) is possible from a set of coexistence points located below the critical point.

In order to ensure that each parameter is determined unambiguously, the following procedure is followed. In a first step, the parameters P_c and γ are estimated by regression from the sole equation (4). This estimation is used to determine the search interval for P_c. Then this interval is sampled with a fine spacing and the other parameters are optimized at imposed P_c: γ is regressed using equation (4), λ and ρ_c are regressed from equation (5), λ_1 and μ are regressed using equation (6), λ_2 is regressed using equation (7) and x_c is obtained through (9). A dimensionless error criterion incorporating densities and compositions is used to define which among all the tested values of P_c yields the best overall result. In this procedure, the optimization is split into steps where no more than two parameters are optimized at the same time. Treating each step by standard linear regression is thus sufficient to implement the method. In figure 1, two examples are shown where this procedure is tested against an experimental data set. In order to reproduce the type of conditions prevailing in molecular simulation, the regression of the eight parameters has been applied to a subset of data corresponding to pressures significantly below the critical point. It can be seen that the critical density, critical pressure and critical composition are correctly extrapolated. As discussed previously [23], care must be taken to the selection of the reference data points in this procedure. Indeed, low pressure points must not be considered as reference data because the Taylor-like expansion of equations (8) and (9) does not hold far away from the critical point.

2.1.4 Intermolecular potentials. Several intermolecular potentials have been proposed in the literature to address the phase equilibrium properties of hydrogen sulphide [70–72], using a Lennard–Jones 6–12 potential and partial electrostatic charges. In the model proposed by Kristof and Liszi [72], which was used in this study, hydrogen sulphide is represented by a single Lennard–Jones site and four electrostatic point charges. The parameters of the model are recalled in [23]. Prior to the present work, this potential has been shown to represent correctly the liquid–vapour equilibrium of the pure compound [73], its viscosity [74], the phase diagrams of its mixtures with methane and water [27] or with light *n*-alkanes [25]. It describes also very well the volumetric behaviour of hydrogen sulphide at high pressure, either pure or mixed with carbon dioxide [27].

In the present study, hydrocarbons have been mainly simulated using the anisotropic united atoms (AUA) intermolecular potential [61,75–77]. Compared with united atoms (UA) potentials, AUA describes as well each carbon atom and its bonded hydrogen atoms by a unique Lennard–Jones center. However, the force center is not located on the carbon nucleus but close to the

Table 1. Simulation of the adsorption of a dehydrated natural gas containing traces of methanethiol and ethanethiol in NaX faujasite at 298 K for two pressures (0.1 and 5 MPa).

		P = 0.1 MPa			*P = 5 MPa*		
	Molar fraction of the gas phase	*Chemical potential/k (K)*	*Molecules per unit cell*	*Molar fraction in adsorbed phase*	*Chemical potential/k (K)*	*Molecules per unit cell*	*Molar fraction in adsorbed phase*
Methanethiol	50 ppm	−6117.5	23	0.130	−4951.75	20	0.098
Ethanethiol	100 ppm	−5910.98	6	0.034	−4745.20	6	0.029
Toluene	100 ppm	−5910.98	<1	<0.006	−4745.2	<1	<0.005
n-Heptane	1000 ppm	−5431.36	–	<0.006	−4265.6	<1	<0.005
CO_2	0.02	−4332.08	1	0.006	−3166.3	<1	<0.005
Propane	0.03	4332.08	<1	<0.006	−3166.3	<1	<0.005
Ethane	0.10	−4059.02	<1	<0.006	−2897.6	<1	<0.005
Methane	0.85	−3197.69	<1	<0.006	−2053.84	<1	<0.005
H_2O	60 ppm	−6063.2	144	0.818	−4897.4	177	0.863
H_2S	4 ppm	−6870.2	<1	<0.006	−5704.42	<1	<0.005
Total			176			205	

geometrical center of the carbon and hydrogen atoms, on the external bisector of the C—C—C angle. This slightly different position of the AUA force center allows to account for the hydrogen atoms, although they are not explicitly represented. Apart from this difference, the construction of the molecule obeys the same rules as UA potentials, i.e. the carbon skeleton is built with the same constraints on bond lengths and similar expressions for intramolecular energy (bending potential and torsion potential).

For hydrocarbons, the AUA potential parameters of the alkyl CH_2 and CH_3 groups have been calibrated from liquid–vapour equilibrium data of a few reference components and it has been subsequently validated on a much larger number of hydrocarbons. In the case of *n*-alkanes, the potential has been calibrated on ethane, *n*-pentane and *n*-dodecane [78].

The AUA parameters for cyclic alkanes have been determined from cyclopentane and cyclohexane and they have been validated on cyclooctane [61].

The AUA parameters for the CH group in aromatics have been determined primarily from benzene [77]. Opposite to alkanes which are considered flexible, the aromatic ring is assumed rigid with hexagonal symmetry. The aromatic carbon group parameters were determined from naphthalene [76]. A more detailed account of the capabilities of the AUA potential is available in [23]. For the present study, we have used the Lorentz–Berthelot combining rule to obtain the Lennard–Jones interaction parameters between unlike groups, in the same way as done when developing the AUA potential. With the exception of the H_2S–benzene system that will be discussed specifically later, no empirical parameter has been used when applying the Lorentz–Berthelot rule.

The OPLS potential has been also used in the present work to investigate the influence of electrostatic energy in the benzene–H_2S system. This potential has been developed for benzene and alkyl-substituted monoaromatics [79–81]. In the case of benzene, every carbon and every hydrogen is represented with a separate Lennard–Jones force center. The structure is considered rigid with hexagonal symmetry. Positive charges are located on the hydrogens and opposite negative charges on the carbon nuclei. This model reproduces very well the liquid density, the cohesive energy and the pairwise distribution function of liquid benzene in ambient conditions. However its description of thermodynamic properties is less accurate at high temperature [77].

2.1.5 Simulation conditions. For the systems which did not display a critical point (i.e. below 373 K), the system size was 200–500 molecules. Selecting the system size and global composition is a delicate aspect in the simulation of the phase diagrams presenting a critical point. The global composition was selected in such a way that both phases had comparable number of molecules on average. In order to avoid density inversion between phases and to eliminate suspicious density fluctuations, it was necessary to increase the size of the system and the total number of molecules, when pressure was increased. For the systems investigated, this appeared necessary for pressures higher than 50% of the critical pressure. By increasing the system size up to 1000–2000 molecules, i.e. the limit of reasonable computing time, it was possible to perform well-converged simulations at pressures as high as 80–85% of the critical pressure in the systems considered.

The simulation length was 20–30 million steps and average properties were taken after a stabilisation period of 2–5 million steps. Typical frequencies of Monte Carlo moves were 0.25 for translations, 0.20 for rotations, 0.05 for configurational bias regrowth, 0.05 for flips, 0.05 for reptations, 0.005 for volume changes and 0.395 for molecule transfers.

The Lennard–Jones interactions were truncated at half the box size and corrected with a standard long range correction. The electrostatic energy was computed using the reaction field method [82,83], assuming the liquid phase to behave as a dielectric with infinite dielectric constant.

2.2 Simulation of the phase equilibrium of H_2S–hydrocarbon

2.2.1 H_2S–*n*-hexane. The phase behaviour of the H_2S–*n*-hexane system has been investigated by Laugier and Richon [84]. In the present study, we will perform the comparison of their experimental measurements with simulation results by the Gibbs ensemble method and by the Gibbs–Duhem integration at the temperature of 422.6 K.

Gibbs ensemble simulations have been performed at the same pressure levels as the experiments between 3.595 and 7.545 MPa and at two additional levels, 7.00 and 7.80 MPa. Gibbs–Duhem integration was initialized with the 3.595 MPa Gibbs ensemble results.

The target pressures for the iterative Gibbs–Duhem scheme have been fixed at the same pressure levels as Gibbs ensemble simulation between 4.575 and 7.80 MPa, with an additional target at 8.20 MPa. In all cases, the pressure obtained by grand canonical simulation for the liquid and vapour phases were compatible with each other, close to the target pressure.

2.2.1.1 Simulation results

The equilibrium phase compositions of the H_2S–*n*-hexane system at 422.6 K obtained with Gibbs–Duhem integration and with the Gibbs ensemble are displayed in figure 2. It appears that simulation results from both methods are in good agreement with experimental data.

The coexisting densities obtained by the two methods are also in good agreement. It may be noticed from figure 3 that the average density between the vapour and the liquid

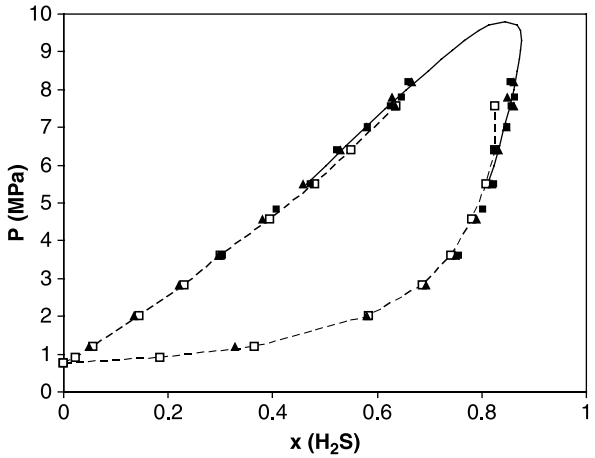

Figure 2. Phase diagram of the H_2S–*n*-hexane system at 422.6 K from experimental measurements (hollow symbols and dashed lines) [84] compared with Gibbs ensemble simulations (filled triangles) and Gibbs–Duhem integration (filled squares). The solid line represents the extrapolation with a near-critical scaling law based on simulation results.

follows approximately a linear trend with pressure. This is an additional justification for using the law of rectilinear diameters (equation (5)) for binary systems.

The critical coordinates of the system, regressed with the near-critical scaling law on the basis of the simulation results between 6.385 and 8.22 MPa, are $P_c = 9.80 \pm 0.20$ MPa, $\rho_c = 304$ kg/m^3, $x_c = 0.845$.

2.2.1.2 Gibbs ensemble vs. Gibbs–Duhem integration

The Gibbs ensemble method and the Gibbs–Duhem integration method provide consistent results and we will discuss now their efficiency for the determination of full phase diagrams, as required for successful industrial applications. Both methods were found to require comparable system sizes to approach sufficiently the critical point. This is logical, as this requirement is due to the larger scale of density fluctuations in liquids which are the same whatever the statistical sampling method. However, the Gibbs ensemble appears somewhat safer with respect to possible convergence problems. It provides indeed independent results for the various pressures investigated, so that an erroneous point is generally detected as outside from the main trend. By contrast, any error committed at some stage of the Gibbs–Duhem integration may propagate its effects to the following pressures and this is likely to be less detectable.

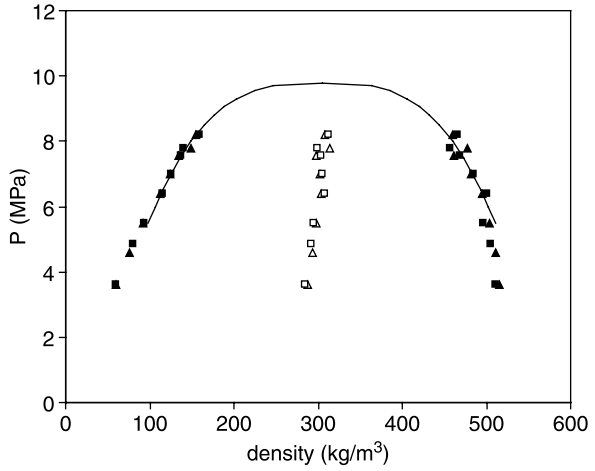

Figure 3. Coexisting densities of the H_2S–hexane system at 422.6 K from Gibbs ensemble simulations (filled triangles) and Gibbs–Duhem integration (filled squares). Hollow symbols represent the average density of liquid and vapour phases and the solid line is the near-critical scaling law regressed on the simulation points.

From a practical standpoint, there are two major differences between these methods. The first is that Gibbs–Duhem integration requires two simulations per state point (one per phase) while Gibbs ensemble requires just one biphasic simulation. Thus Gibbs–Duhem requires thus more time to launch the simulations and to analyze their results. The second difference is that Gibbs ensemble simulations may be processed in a parallel way while the Gibbs–Duhem integration is iterative. With the latter method, the two simulations in the liquid and vapour phases may be processed together for a given target pressure but the simulations for the next target pressure can start only when the results from the previous step have been processed and analyzed. If a cluster of several tens of processors is available, as is the case in IFP and in most molecular simulation groups, the Gibbs ensemble method is faster because the simulations for all pressures can be started simultaneously and the method makes thus a better use of parallel computers. As a result, Gibbs ensemble was selected for the rest of the study.

2.2.2 H_2S–*n*-pentane. The densities and compositions of coexisting liquid and vapour phases of the H_2S–*n*-pentane are known from experiments [85]. Comparison with these data has been performed at the temperature of 344.3 K, using the Gibbs ensemble method at imposed pressure. The size of the simulated system was comprised between 200 molecules at low pressure and 500 molecules at higher pressures, close to the saturation pressure of hydrogen sulphide.

The results (figure 4) indicate a satisfactory match with experimental data. The liquid densities appear somewhat overestimated, a consequence of the slight overestimation (1–2%) of the liquid density of liquid *n*-alkanes by the AUA potential.

2.2.3 H_2S–*n*-pentadecane and H_2S–*n*-eicosane. Gibbs ensemble simulations have been performed on the H_2S–pentadecane and H_2S–*n*-eicosane binary systems at 422.6 K up to 12.0 and 13.0 MPa respectively, in order to compare with experimental data of Refs. [84,86]. The system size was comprised between 300 molecules at low pressure to 1200 molecules at the higher pressure investigated. As is the general case with mixtures

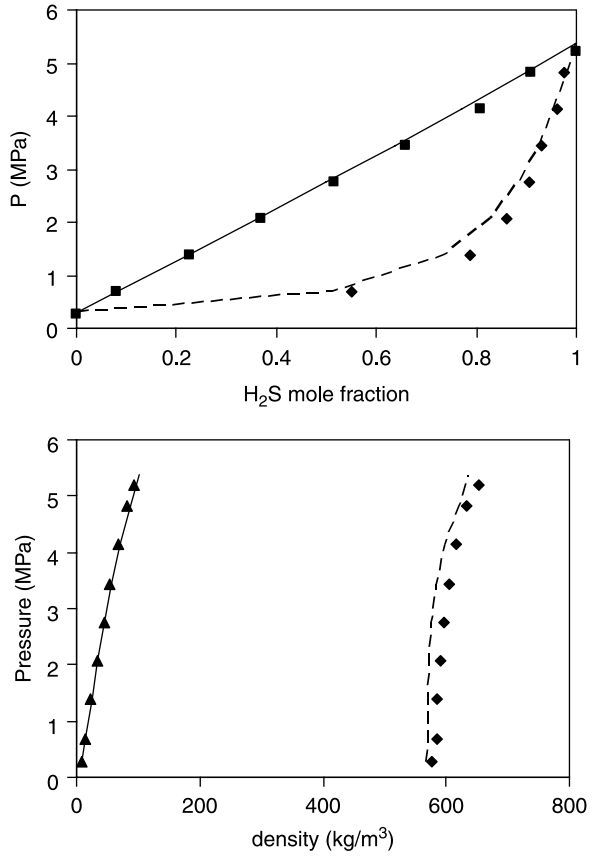

Figure 4. Liquid–vapour phase diagram (top) and coexisting densities (bottom) of the H_2S–*n*-pentane system at 344.3 K from simulations (filled symbols) and experimental measurements [85] (solid and dashed lines).

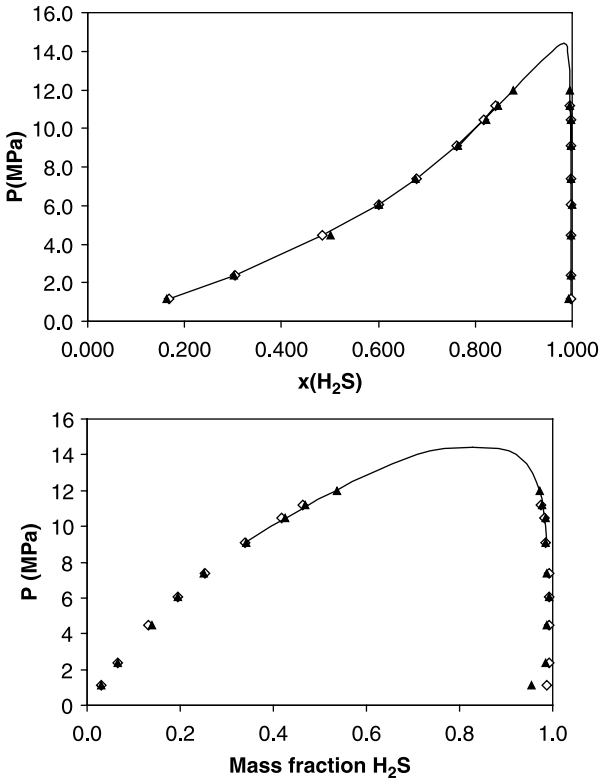

Figure 5. Phase diagram of the *n*-pentadecane–H_2S system at 422.6 K from simulations (filled symbols) and experiments (hollow symbols and dashed line). The same results are expressed in mole fraction (top) and mass fractions of hydrogen sulphide (bottom).

displaying a strong difference of molecular weights, the phase envelope is highly asymmetric when the pressure–composition diagram is expressed with respect to mole fractions (figure 5, top). The composition of the vapour phase is better seen when the diagram is expressed in terms of mass fractions (figure 5, bottom and figure 7). This allows to see that the alkane content of the vapour phase is significantly lower in the H_2S–*n*-eicosane (figure 7) than in the H_2S–*n*-pentadecane system (figure 5), an expected consequence of the lower vapour pressure of *n*-eicosane. Whatever the representation, the known part of the phase diagrams, i.e. the liquid composition, is very well predicted. Two procedures were used to estimate the critical point, either on the basis of mole fractions or mass fractions. It may be noticed that the critical pressure of the H_2S–*n*-pentadecane mixture is the same, whether the mass fractions or the mole fractions are used to regress the critical coordinates (figure 5). This suggests that the coexisting density curve (figure 6) is controlling the near-critical extrapolation more firmly than the phase compositions. The estimated coordinates of the critical point are $P_c = 14.4 \pm 0.2$ MPa, $\rho_c = 409$ kg/m^3 and $w_c = 0.83$ for the H_2S–*n*-pentadecane system and $P_c = 15.2 \pm 0.2$ MPa, $\rho_c = 433$ kg/m^3 and $w_c = 0.82$ for the H_2S–*n*-eicosane system.

2.2.4 H_2S–cyclohexane. The H_2S–cyclohexane system has been simulated at 323 and 422.6 K, two temperatures for which experimental measurements are available from Laugier and Richon [84]. At the temperature of 323 K, the system comprised 300 molecules. At the temperature of 423 K, the system size has been increased from 300 molecules at low pressures up to 1400 molecules in order to investigate conditions up to 9 MPa, sufficiently close to the critical point to allow a reliable regression of the parameters of the near-critical scaling laws.

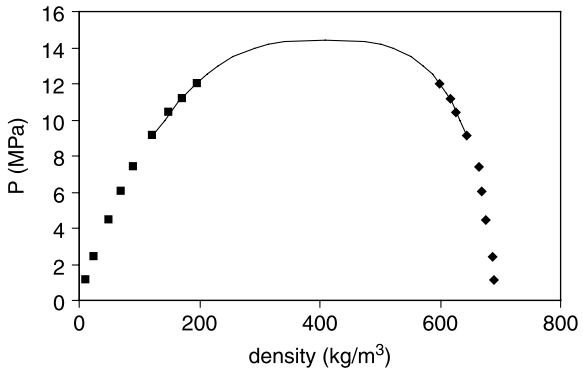

Figure 6. Coexisting densities of the vapour and liquid phases in the H_2S–*n*-pentadecane system at 422.6 K. The solid line is the extrapolation with the near-critical scaling expression.

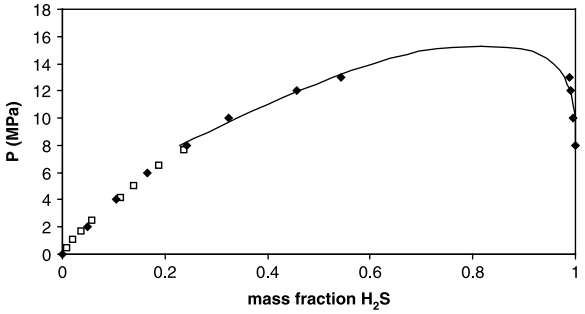

Figure 7. Phase diagram of the *n*-eicosane–H_2S system at 422.6 K from simulations (filled symbols) and experiments (hollow symbols). The solid line is the extrapolation of simulation results with a near-critical correlation.

The outcome of the simulation (figure 8) indicates a good agreement with experimental data, although the phase envelope seems somewhat too large at 323 K.

2.2.5 H_2S–benzene. The benzene–H_2S system has been simulated with the AUA potential at 422.6 and 323 K. As summarized by figure 9, the comparison with experimental data [84] shows that the H_2S content of the liquid phase is significantly underestimated with this potential. It is suspected that this deviation is caused by the insufficient account of electrostatic energy. In H_2S–H_2S interactions, the electrostatic interactions between dipole moments are explicitly considered. In the AUA potential of benzene, the quadrupolar interaction between benzene molecules is implicitly taken into account in the Lennard–Jones

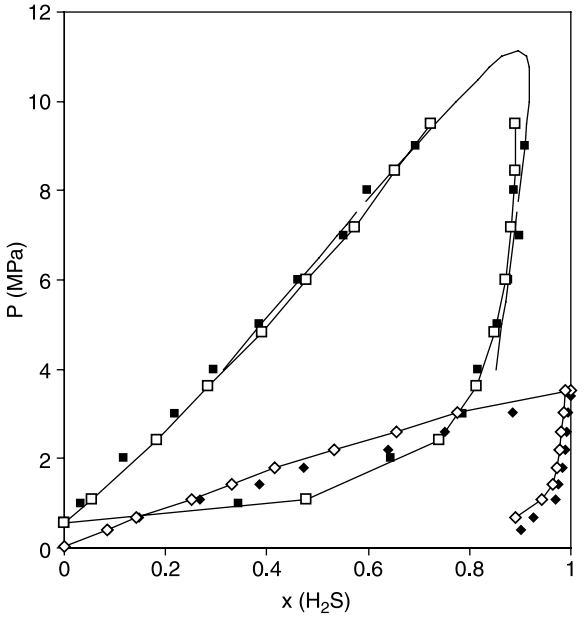

Figure 8. H_2S–cyclohexane phase diagrams at 323 K (diamonds) and 422.6 K (squares) from simulations (filled symbols) and from experimental measurements [84] (hollow symbols and dashed lines). The solid line represents the extrapolation of simulation results with a near-critical scaling law.

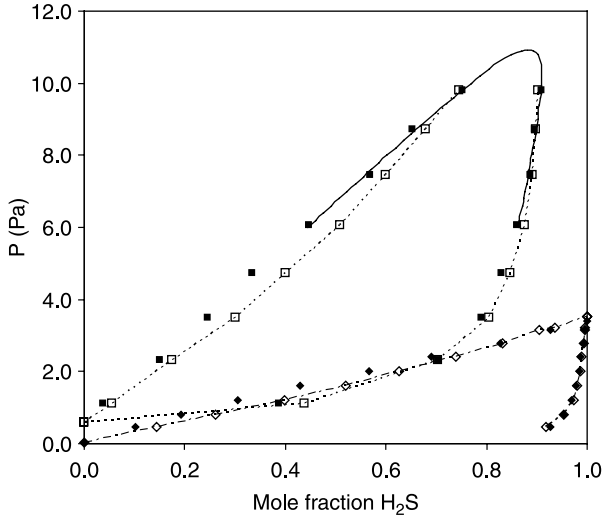

Figure 9. H_2S–benzene phase diagrams at 323 K (diamonds) and 422.6 K (squares) from simulations using the AUA potential without group interaction coefficient (full symbols) and from experimental measurements [84] (hollow symbols and dashed lines). The solid line represents the extrapolation with a near-critical scaling law.

parameters. However, the interaction between the dipole moment of hydrogen sulphide and the quadrupole moment of benzene is neither taken into account implicitly nor explicitly. It is therefore logical to try a benzene model that considers explicitly electrostatic energy. As the average electrostatic interactions are always attractive (i.e. negative), such a model is expected favour the miscibility of the liquid and vapour phases, i.e. it should restrict the extent of the two-phase region as observed.

The benzene–H_2S system has been thus simulated with the OPLS potential in the same conditions as the AUA potential. At the temperature of 323 K, a total number of 300 molecules was used. For the temperature of 422.6 K, the total number of molecules was progressively increased from 300 to 1000 when the pressure was increased from 2.33 to 8.70 MPa, in order to maintain fluctuations small, so that the results are unlikely to depend on box size. Compared with the AUA potential, the computing time was increased by a factor 5 at least. The simulations with a large number of molecules close to the critical pressure required more than a full week of computation. The simulation results are indicated by figure 10. For the temperature of 422.6 K, the critical densities and molar fractions were correlated on the basis of the simulation results obtained in the range 6–9.8 MPa. The regressed critical coordinates are $P_c = 11.3 \pm 0.2$ MPa, $\rho_c = 364$ kg/m^3, $x_c = 0.90$.

As expected, the two-phase region is narrower with OPLS than with the AUA potential. The H_2S content of the liquid phase is slightly overestimated, while it is generally underestimated in the vapour phase. Compared with the AUA potential, the overall behaviour is improved, without needing any specific interaction parameter. The critical coordinates are somewhat changed with OPLS, as compared with the AUA potential. For instance, the critical pressure is changed from 10.9 to 11.3 MPa and the critical density from 359

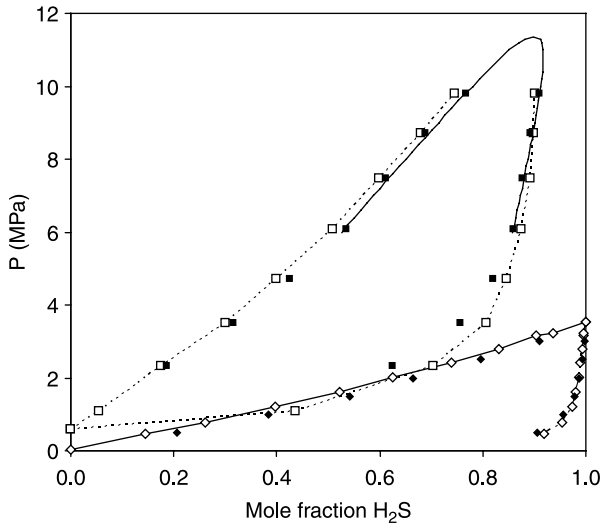

Figure 10. Phase diagram of the H_2S–benzene binary system at 323 K (diamonds) and 422.6 K (squares) from simulations with the OPLS potential (filled symbols) and from experiments [84] (hollow symbols and dashed lines). The solid line represents the extrapolation of simulation results with a near-critical scaling law.

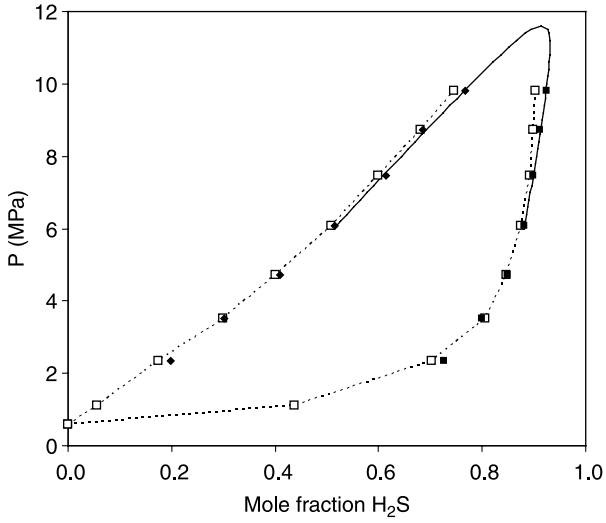

Figure 11. Benzene–H_2S phase diagram at 422.6 K (squares) from simulations using the AUA potential with a group interaction coefficient $k_{ij} = -0.05$ (filled symbols) and from experimental measurements [84] (hollow symbols and dashed lines). The solid line represents the extrapolation of simulation results with a near-critical scaling law.

to 364 kg/m^3. However these changes are not much larger than the uncertainty of their determination, which is estimated to 0.2 MPa and 5 kg/m^3.

Although successful, the OPLS potential would be difficult to extend to aromatics other than the methylated derivatives of benzene. For instance, the mixtures of H_2S with long chain alkylbenzenes or naphthalene could not be considered without an adequate parametrization and would require very long computing time. Computing time being a severe limiting factor when using the OPLS potential in near-critical conditions, it is tempting to adapt the AUA potential in such a way that it represents better the phase behaviour of the binary system benzene–H_2S.

As the AUA potential predicts an excessive extent of the two-phase region (figure 9), an improvement should be possible by increasing the attraction energy between the benzene and hydrogen sulphide molecules. It is therefore proposed to use a negative value of the group interaction parameter k_{ij} in the Lorentz–Berthelot combining rule on the cross Lennard–Jones energy parameter.

$$\varepsilon_{ij} = \sqrt{\varepsilon_i \varepsilon_j}(1 - k_{ij}) \tag{10}$$

By trial and error, it has been found that an optimum value $k_{ij} = -0.05$ is adequate for improving significantly the liquid phase compositions at both temperatures, without altering the description of the vapour phase branch (figure 11). For the temperature of 422.6 K, the estimated critical coordinates are $P_c = 10.9 \pm 0.2$ MPa, $\rho_c = 359$ kg/m^3, $x_c = 0.88$.

2.2.6 Prediction of unknown systems. Using the AUA potential tested on the binary mixtures discussed above, simulations have been conducted on numerous binary and quaternary systems for which no experimental data are available. The binary systems include H_2S–*n*-pentacosane, H_2S–ethylbenzene, H_2S–*n*-butylbenzene, H_2S–*n*-hexylbenzene, H_2S–*n*-dodecylbenzene, H_2S–cyclopentane, H_2S–*trans*-decalin, H_2S–tetralin and H_2S–naphthalene. The quaternary system was a mixture of methane, CO_2, H_2S and *n*-heptane. The full phase envelopes were determined for the binary systems at two temperatures, providing useful phase equilibrium and density data for the validation and refinement of engineering equations of state. As an example, we present the H_2S–ethylbenzene phase diagram obtained by simulation (figure 12). The AUA potential parameters have been taken identical to the pure alkylbenzenes [75,76]. The Lorentz–Berthelot combining rule has been used without group interaction coefficients, except between H_2S and the aromatic CH, for which the

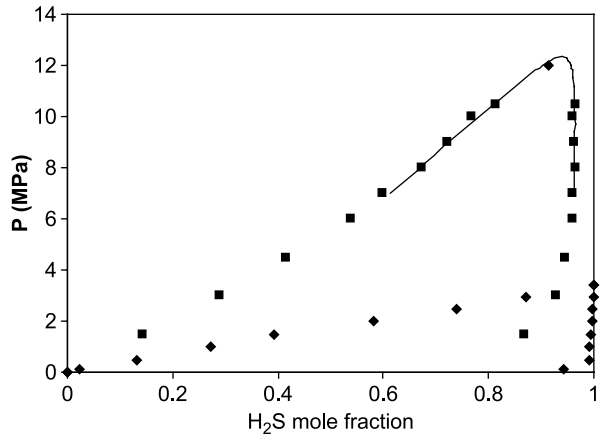

Figure 12. H_2S–ethylbenzene phase diagram at 323 K (diamonds) and 422.6 K (squares) predicted from simulations using the AUA intermolecular potential. The solid line represents the extrapolation of simulation results with a near-critical scaling law.

value obtained from the analysis of the H_2S–benzene mixture ($k_{ij} = -0.05$) was used. When compared with the H_2S–benzene system at the same temperatures, this diagram illustrates the progressive shift of the phase envelope towards higher molar concentration of H_2S and the slight increase of critical pressure with increasing carbon numbers.

More importantly, the determination of the critical coordinates for each system in a large range of carbon number has allowed us to characterize the increasing trend of critical pressures with increasing carbon numbers. This information is very important in the light of H_2S reinjection in oil-bearing reservoirs, because it allows to know whether oil–H_2S mixtures, in which high molecular weight compounds are present, will be monophasic or not. If the system is monophasic over the whole H_2S concentration range, fluid flow in porous media is qualitatively different and enhanced oil recovery is expected.

Beyond reservoir engineering, other applications of H_2S–alkane phase equilibria can benefit from the present study. A first example is the prediction of H_2S–hydrocarbon phase equilibria in the conditions of hydrocracking, i.e. at temperatures so high (400°C) that hydrocarbons are too unstable for considering reliable measurements [87]. Simulation results have been used to calibrate the parameters of the Grayson–Streed correlation which would be otherwise unphysical when applied to H_2S–hydrocarbon systems at high temperatures. A second example is the solubility of high pressure gases in polyethylene, which is of industrial interest because it influences the barrier properties of this material in flexible pipes used for oil and gas transport [23]. Assuming that the crystalline part of the material does not absorb gases, molecular simulation can provide useful results for understanding solubility variations as a function of gas pressure and composition, among other parameters.

3. Adsorption in zeolites

3.1 Simulation methods

The results shown in this article have been obtained by grand canonical Monte Carlo simulation, considering the aluminated siliceous framework as immobile. Cations may be either considered as a mobile species, in the same way as guest molecules, or as fixed. In all cases, the interaction energy of mobile species with the fixed framework are computed at the nodes of a fixed grid with regular spacing, which covers the whole unit cell. Interpolating between these tabulated energies allows for an efficient simulation of the grand canonical ensemble (figure 13).

The following contributions to the potential energy are considered:

- dispersion and repulsion energy,
- bending and torsional energy of flexible molecules such as *n*-alkanes,
- electrostatic energy, using point charges on the framework and on molecules, and
- polarization energy, arising from the polarization of mobile species in the electric field created by the zeolite and by surrounding species.

Dispersion and repulsion are modelled with a Lennard–Jones 6-12 functional form for neutral mobile species. We use either All Atoms in the case of aromatics [80] or CO_2 [88], UA in the case of water [89] and AUA in the case of

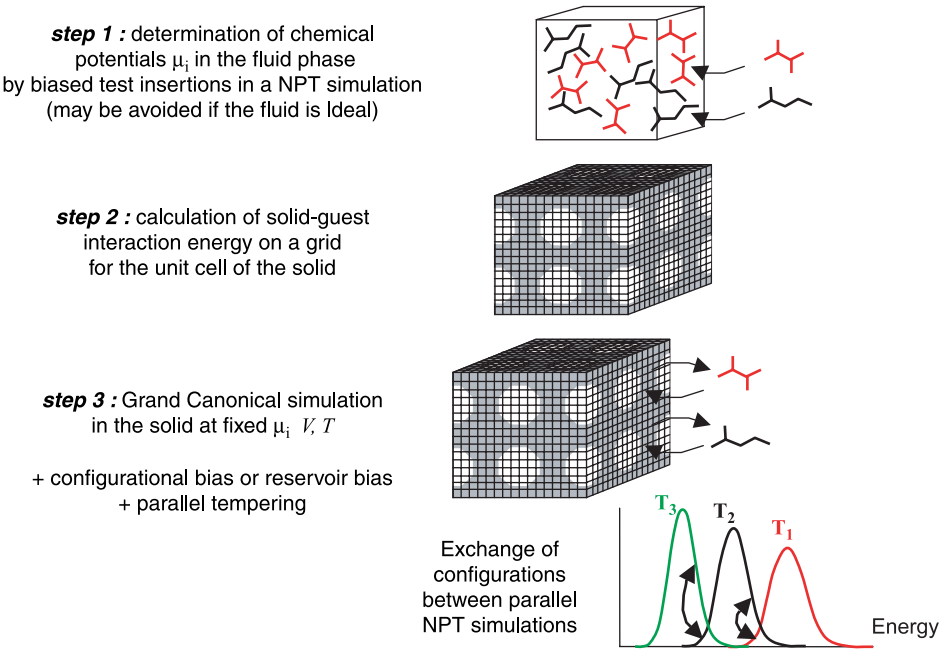

Figure 13. General approach of Monte Carlo simulation of the adsorption in zeolites from non-ideal fluid phases.

organic compounds like alkanes or alkanethiols [62,78,90]. A Buckingham exp-6 potential [45] is used in the specific case of cation–framework interactions.

Electrostatic energy is neglected when non-polar molecules like alkanes are considered, but it is included when the mobile species bear significant charges (cations), dipole moments (thiols, water, ...) or quadrupole moments (CO_2).

Polarization energy is not accounted for when purely siliceous forms are considered, because the electric field is small in these cases due to the absence of charge-compensating cations. It is explicitly considered in cation-substituted zeolites, such as faujasites. Electrostatic energy and polarization energy are computed with Ewald summation [21] using the charge distributions obtained by electronegativity equalization method by Mortier *et al.* [91,92].

The Monte Carlo moves used to sample efficiently the configuration space in grand canonical simulations are as follows:

- rigid body translations,
- rigid body rotations,
- regrowth of flexible molecules, using the configurational bias [59,93] and reservoir bias [34] schemes,
- insertions of new molecules or deletion of existing molecules, using configurational and reservoir bias for linear and branched molecules or a two-step reservoir bias involving a pre-insertion [61] for rigid or cyclic molecules,
- swap, i.e. identity exchange between two molecules,
- jump, i.e. destruction of a molecule at one place and biased insertion at a randomly selected place in the simulation box, using configurational bias or reservoir bias depending on the type of molecule, and
- exchange of temperatures or chemical potentials between two parallel simulations, according to the classical parallel tempering scheme [94].

In order to evaluate the chemical potential of every molecular species when adsorption is considered far from ideal gas conditions, a preliminary *NPT* simulation of the fluid phase is conducted at the desired equilibrium pressure with biased Widom test insertions (figure 13). The GIBBS software used for our calculations allows for grand canonical simulations of adsorption and *NPT* simulations of fluid phases with the same algorithms, so that full consistency is ensured. Among the above moves, jump moves appear to be essential for the efficient finding of equilibrium cationic locations. Compared with our previous investigations [43], they allow for a quicker convergence without requiring exploration of higher temperatures.

3.2 Applications

3.2.1 Location of cations in Na faujasite. In figure 14, we show the experimental and simulated distribution of non-framework cations among the different types of crystallographic sites in faujasites with various silicon to aluminium ratios, using the intermolecular potential of Auerbach and coworkers [45]. Thanks to the jump move, the sequential filling of sites II, I, I′ and III is well described with significantly reduced computational effort. Sites II are first occupied because they are more energetically favorable. Once all the 32 sites II present in a unit cell are occupied, following cations take place in sites I where their energy is higher. There are only 16 sites I and the next favorable sites are sites I′. However, electrostatic repulsion prevents sites I and I′ from being occupied simultaneously. From an energetic standpoint, it is more favorable that the further increase in the number of cations causes progressively sites I to be abandoned while twice as many sites I′ are occupied. When the 32 sites I′ are occupied (i.e. when the total number of cations is 64, including sites II), there are no more cations in sites I. Further cations occupy sites III, which are even less favorable than II, I and I′. Finding this sequence as a result of a simple force field is encouraging for more complex applications involving guest molecules.

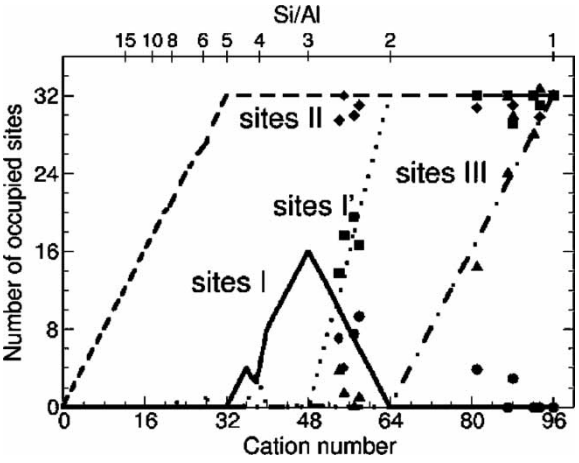

Figure 14. Occupation of cationic sites I, I′, II and III in anhydrous sodium faujasites for various numbers of cations per unit cell, i.e. for various Si/Al ratios. Continuous lines indicate simulation results [96] for sites I (solid lines), I′ (dotted lines), II (dashed line) and III (dot-dashed line). Experimental data are indicated by dots (sites I), squares (sites I′), diamonds (sites II) and triangles (sites III).

3.2.2 Adsorption of alkanes. In zeolites with low polarity, such as silicalite or ferrierite, the adsorption of hydrocarbons may be described by considering exclusively dispersion and repulsion forces through a Lennard–Jones potential [35]. In this approach, alkanes are treated as chains of UA where each CH_2, CH_3 or CH group is treated as a separate Lennard–Jones centre, neglecting hydrogens in the same way as in the simulation of liquid–vapour equilibrium [59]. Using the AUA model has proved very efficient to describe the adsorption of alkanes in silicalite [38] as illustrated in figure 15 and ferrierite [40]. In this model, the interaction between the zeolitic oxygens and the force centers of the guest molecules is

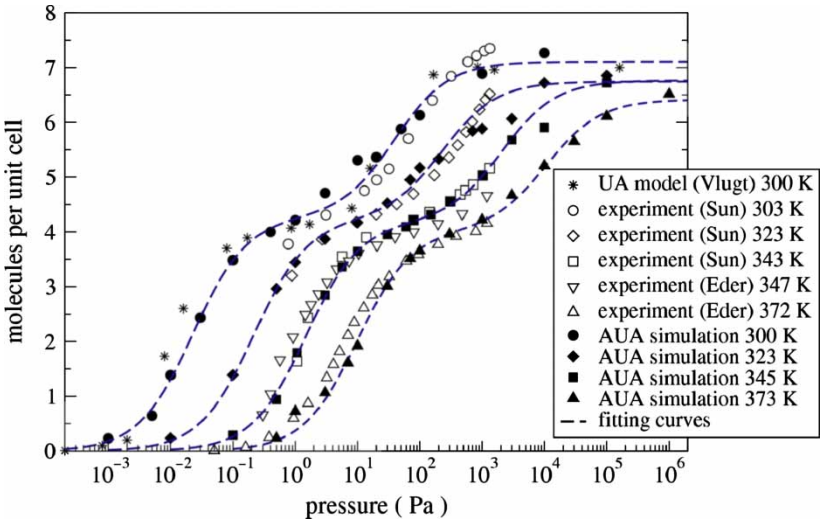

Figure 15. Adsorption isotherms of *n*-heptane in silicalite-1 at 300, 323, 345 and 373 K after Pascual *et al.* [38]. Hollow symbols, experiments [113]; stars, UA model of Vlugt *et al.* [35]; filled symbols, AUA model; and dotted lines, Langmuir dual site correlation model.

determined from the Lorentz–Berthelot combining rule based on standard Lennard–Jones parameters for the framework oxygens ($\sigma = 3.00$ Å, $\varepsilon/k = 93.53$ K). Thus the model may be used without further calibration to model the adsorption of other compounds in silicalite like alkenes [39]. The S-shaped adsorption of *n*-heptane in silicalite seen in figure 15 may be explained by a detailed analysis of molecular positions [35,38]. The lower slope observed at four molecules per unit cell, i.e. half of the saturation plateau, is explained by the transition from a favorable adsorption up to four molecules per unit cell in sinusoidal channels, while further filling of straight channels is hampered by the occupancy of intersections. As there is no drastic change of the isosteric heat of adsorption above four molecules per unit cell, this effect may be considered mostly entropic.

The application of this model to the adsorption of alkanes in cation-exchanged faujasites is not straightforward. Indeed, it appears that the Lennard–Jones potential alone underestimates significantly the attraction energy between alkanes and faujasites. The explanation that we propose for this failure is that the electrostatic field is considerably more important in these zeolites, so that polarisation energy cannot be neglected as in silicalite and ferrierite. Faced with this problem, it has been proposed to attribute a very attractive potential to the dispersion–repulsion interactions between cations and guest alkanes [95]. This allows a successful description of adsorption isotherms, but it is not certain that this implicit account of polarization will not produce artifacts. For instance, Calero *et al.* predict a substantial reorganization of cations upon the adsorption of *n*-alkanes and this effect might be exaggerated if the actual polarization energy turns out to be more evenly distributed in the zeolite than considered in their model. The alternative strategy that we propose is to account explicitly for the polarisation energy, which can be evaluated by using the average dipole polarisabilities of alkanes [26]. As illustrated by the Henry constants of *n*-alkanes in $Na_{52}Y$ faujasite shown in figure 16, this approach is providing encouraging results without calibrating any new parameter. This might be a general alkane adsorption model, encompassing silicalite, ferrierite and NaY faujasite in a single theoretical framework with a unique parametrization. Further extension of this line of research to other systems is under way.

3.2.3 Adsorption of water. Using the simple TIP4P model of water [89] and the same cation force field as above [45], it is possible to simulate the adsorption of water in sodium-exchanged faujasites. For this purpose, we describe dispersion–repulsion energy between water and framework oxygens with the same model as alkanes. As it is based on a combining rule between TIP4P and Pascual's parameters [38] no specific parameter has to be calibrated. Electrostatic energy is computed by the simple application of Coulomb's law with the same zeolite charges as in the

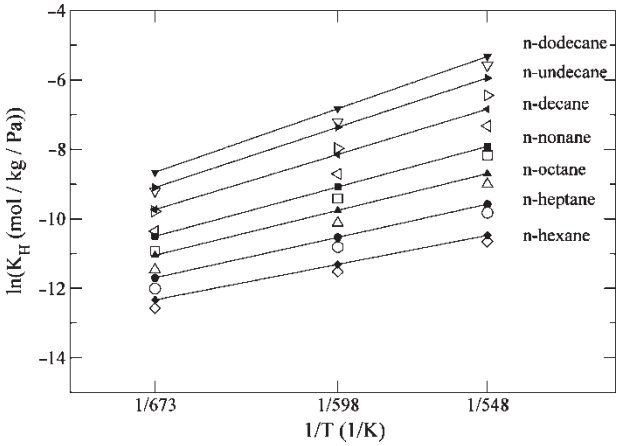

Figure 16. Henry constants of linear alkanes in sodium faujasite $Na_{52}Y$ obtained by simulation [114] (hollow symbol) and compared with experimental data [115] (solid lines and filled symbols). The statistical uncertainty is smaller than the symbol size.

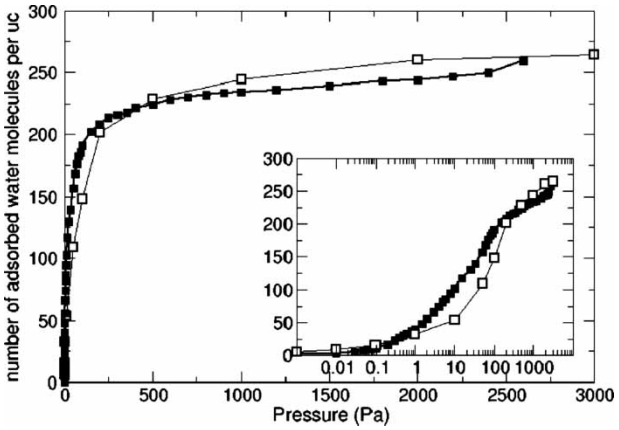

Figure 17. Adsorption isotherm of water in $Na_{52}Y$ faujasite at 300 K. Hollow symbols, simulation results [96]; solid symbols, experiments [116].

above investigation of cation positions and TIP4P original charges. Given the simplicity of this approach, the outcome of this simulation is surprisingly good, as illustrated by the adsorption isotherm of water in $Na_{52}Y$ faujasite [96] shown in figure 17. In agreement with experimental findings from X-ray diffraction, cations are found to move from sites I to I′ when water is adsorbed [96]. The reason behind this motion of cations is that water in sodalite cages attract cations in sites I′ through dipolar interactions which are much weaker if cations stay in sites I. This kind of understanding is encouraging for the further investigation of water influence upon the adsorption selectivity of aromatic isomers in faujasites.

3.2.4 Adsorption of thiols from natural gas. Alkanethiols (R-SH, where R is methyl, ethyl or propyl) are trace components of natural gas that are highly poisonous and strongly smelling. Adsorption is considered as one of the possible way to remove these compounds from natural gas, as required by existing regulations. They are polar compounds for which an AUA model has been proposed [90], using atomic electrostatic charges determined from *ab initio* simulations. A simplified potential for alkanethiols has also been proposed in which the electrostatic charges were restricted to the vicinity of the SH group [23]. In order to simulate the adsorption of alkanethiols, we can thus use the same approach as followed above with water, i.e. dispersion–repulsion energy from Pascual's approach [38] and electrostatic energy from Coulomb's law. This allows a reasonable description of the adsorption isotherms of ethanethiol [23]. When adsorption from a multicomponent gas mixture under high pressure is considered, the same grand canonical approach can be used, provided chemical potentials are determined appropriately by Widom test insertions (figure 13). Doing this, the same approach as above is used for water and hydrocarbons. In table 1, we provide a typical result of such simulations in NaX faujasite for a dehydrated natural gas containing 98% of hydrocarbon gases, 150 ppm of alkanethiols and also traces of other compounds (water, liquid hydrocarbons and acid gases). Due to the importance of its electrostatic interactions with the zeolite, water is strongly adsorbed, despite its low concentration in the gas (60 ppm). Alkanethiols are second among adsorbed products, which is logical as their electrostatic interactions are weaker than water. The other species are not significantly adsorbed, although they are by far major in the fluid phase. These results are preliminary because polarisation energy was not accounted for and aromatics were considered non-polar. Nevertheless, experimental investigation has shown that simulation has well identified the privileged adsorption of polar compounds in this system—particularly water—despite their low concentration and low molecular weight. This is encouraging for further use of simulation for adsorbent screening.

4. Transport properties of *n*-alkanes at high pressure

4.1 Determination of viscosity from equilibrium MD

The computation of the shear viscosity is carried out through the Einstein relation, which overcomes the effect of long time decay of the pressure tensor–time correlation function in theoretically equivalent Green–Kubo calculations. The Einstein relation employed in this work is described by Smith and van Gunsteren [97]. However, unlike the original work, we use all the elements of the stress tensor to improve convergence and statistics [98]. The viscosity coefficient is then given by the expression

$$\eta = \frac{1}{20}\frac{V}{k_B T}\lim_{t\to\infty}\frac{\mathrm{d}}{\mathrm{d}t}\left[\sum_{\alpha}\left\langle \Delta P^{T}_{\alpha\alpha}(t)\right\rangle^2 + 2\sum_{\alpha>\beta}\left\langle \Delta P_{\alpha\beta}(t)\right\rangle^2\right] \tag{11}$$

Here, α and β are indices running over the three Cartesian coordinates, V is the volume, T is the temperature and $\Delta P_{\alpha\beta}(t)$ denotes the displacement of the elements of the pressure tensor $P_{\alpha\beta}$ according to

$$\Delta P_{\alpha\beta}(t) = \int_0^t \frac{1}{2}\left(P_{\alpha\beta}(\tau) + P_{\beta\alpha}(\tau)\right)\mathrm{d}\tau \tag{12}$$

and

$$\Delta P^{T}_{\alpha\beta}(t) = \int_0^t \left(P_{\alpha\alpha}(\tau) - \frac{1}{3}\sum_{\beta}P_{\beta\beta}(\tau)\right)\mathrm{d}\tau \tag{13}$$

The microscopic expression for the elements of the pressure tensor $P_{\alpha\beta}$ appearing in the integrand of

equations (12) and (13) are given by

$$P_{\alpha\beta}(t) = \frac{1}{V}\left(\sum_i \frac{p_{\alpha i}(t)p_{\beta i}(t)}{m_i} + \sum_{i<j}\sum f_{\alpha ij}(t)r_{\beta ij}(t)\right) \quad (14)$$

In equation (14), p_i is the α-component of the momentum of particle i, $f_{\alpha ij}$ is the α-component of the force exerted on particle i by particle j and $r_{\beta ij}$ is the β-component of the particle–particle vector, $r_{ij} \equiv \mathbf{r}_j - \mathbf{r}_i$. The viscosity is obtained from equation (11), always after some initial time during which the displacement is not a linear function of the time.

From a practical point of view, viscosity computation is possible with an accuracy of a few percents when it is lower than 1 mPa s. When fluids of higher viscosity are considered, the simulation length must be increased to sample the relevant relaxation times. As this is generally associated with a more complex structure, computer time is then a limiting factor. For typical cases, viscosity determination is possible up to 10–20 MPa s with existing scalar MD algorithms.

4.2 Optimization of the AUA potential for *n*-alkanes

Before considering the optimization of intermolecular potentials for *n*-alkanes, it is worth indicating why existing intermolecular potentials are still requiring improvements. In their test of the TraPPE potential, which relies on UA, Kioupis and Maginn [56] have shown that the increase of viscosity with increasing pressure was qualitatively predicted, but the viscosity of *n*-octane was underestimated by 20–30%. MD simulations performed by Dysthe and coworkers [52] have found significant underestimation of the viscosity of dense *n*-alkane liquids with UA potentials and with Toxvaerd's initial parameterization of the AUA potential. In a recent work, the viscosity of *n*-alkanes computed with an alternative parameterization of the AUA potential [78] appeared satisfactory for ethane, with deviations lower than 10%, but under predicted by 20–40% for *n*-pentane and *n*-dodecane [24]. This under prediction is consistent with the over prediction of the self-diffusion coefficient of liquid *n*-hexane with the same AUA potential [78]. Indeed both tendencies indicate that relaxation is too fast. Zhang and coworkers [99] have optimized the parameters of an AUA potential to improve viscosity predictions in the liquid state. However these authors neither test the volumetric behavior nor the liquid–vapour phase equilibrium of the new model, which is likely to be significantly changed as the optimized parameters (group diameters and attraction parameters) are known to exert a significant influence on equilibrium properties. For applications—particularly those considering mixtures with supercritical compounds—it is however important that phase equilibrium and volumetric properties are predicted consistently, because viscosity is known to be strongly correlated with fluid density. All Atoms potentials have been also tested for viscosity prediction in the *n*-alkanes series [52], however in a more limited range of carbon numbers because computing time is then a more stringent limitation. All Atoms potentials did not perform better than UA models for viscosity prediction.

From this overview, it may be concluded that the present level of accuracy of intermolecular potentials is sufficient for qualitative studies, such as the influence of branching [55,56] or the investigation of the non-Newtonian behavior [100] but more quantitative models are clearly desirable for predicting the Newtonian shear viscosity for industrial applications.

In order to improve the AUA potential for the viscosity prediction of *n*-alkanes, we have recently proposed [101] to modify the AUA potential parameters in such a way that the transport predictions are improved and the equilibrium properties are little affected. For this purpose, we take advantage of the influence of the torsion potential on the viscosity behaviour, which is documented in previous studies [102]. From this work, it is expected that the shear viscosity is lower if no torsional energy is considered. It is known that for the temperature range considered in the present work—up to 700 K—the most frequent configurations are close to the torsion energy minima, i.e. *trans* or *gauche* conformations [62]. Thus it may be conjectured that the equilibrium properties of the fluid will not change significantly if the height of the torsional energy barriers are changed, provided the *trans* and *gauche* minima of the torsion energy potential are unchanged. It was thus found that increasing the height of the torsion energy barriers by 40% for the end segments and by 15% for the other segments was sufficient to increase significantly the shear viscosity of *n*-alkanes [101]. As expected, the changes to the phase equilibrium properties of *n*-alkanes were very minor. In figure 18, viscosity predictions are shown for *n*-octane at the temperature of 347.52 K, for pressures up to 360 MPa. With the new torsion potential, the AUA

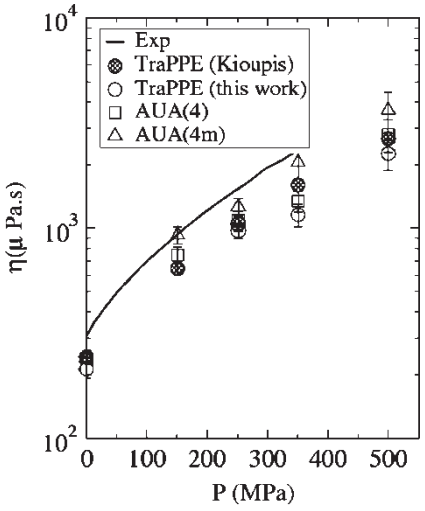

Figure 18. Shear viscosity of *n*-octane at 347.52 K with the Trappe potential [56], with the AUA(4) potential parameters [78] and with the AUA(4m) potential with modified torsion parameters [101]. The continuous line shows the experimental measurements [117].

potential predicts viscosity with substantially lower deviations than the unchanged AUA potential and the TraPPE potential. In figure 19, the density and viscosity of *n*-dodecane are shown in a large range of pressures (up to 160 MPa) and temperatures (from 300 to 470 K). While liquid density is unchanged with the new torsion parameters, viscosity is significantly improved. Similar tests performed on *n*-pentane and *n*-eicosane have also shown significant improvement on the whole temperature and pressure range. Logically, the same model has significantly improved the prediction of the self-diffusion coefficient of *n*-hexane. The new AUA potential permits also to obtain more reliable results of the viscosity in mixtures, particularly in systems with industrial interest. In figure 20, the comparison between our simulations results and the experimental data of Cullik *et al.* [103] for viscosity of the mixture of CO_2 and *n*-decane at 311 K and 34 MPa is shown. We have also compared our simulations with the results obtained by Dysthe *et al.* [104] for the same system employing a previous version of the AUA potential [105]. In this case, the performance of the new potential is considerably better than the previous version of the AUA model when compared to the experimental data.

A very interesting application of this potential is the calculation of the viscosity of alkane mixtures with H_2S at high pressure, for which no experimental data exist as far as we know. Considering that the model has been validated by phase equilibrium data on mixtures, as shown in the first part of the present work, by viscosity data on pure H_2S [74] and by transport properties pure *n*-alkanes [101], there is a small risk that it provides unphysical results when applied to the viscosity of H_2S–*n*-alkane mixtures. For the project considered, obtaining reliable experiments at high pressure was not possible in due time. Molecular simulation has provided useful viscosity predictions within a few months, thus filling a critical gap.

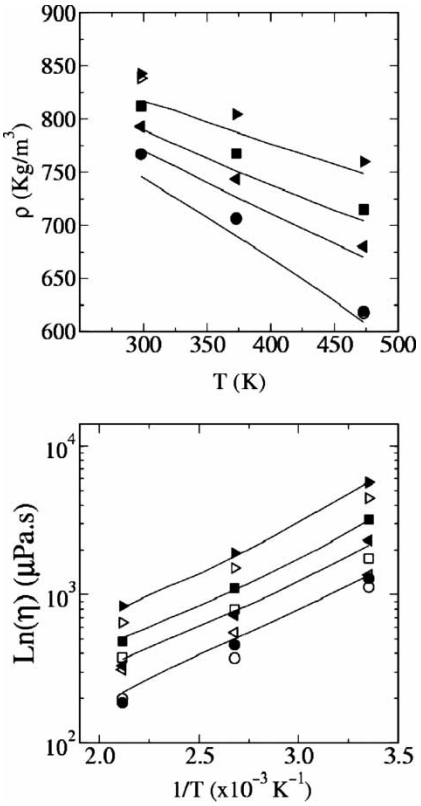

Figure 19. Comparison of simulation results for the density (top) and viscosity (bottom) of *n*-dodecane [101] obtained with the AUA(4) potential (hollow symbols) and the AUA(4m) potential with modified torsion parameters (filled symbols). Experimental data [118] are shown as solid lines. Here, results for four different isobars are presented (from bottom to top on each figure) 0.1 MPa (○), 41 MPa (◁), 81 MPa (□) and 152–160 MPa (▷).

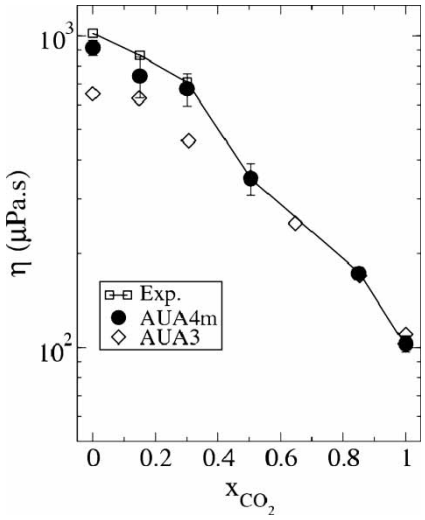

Figure 20. Variation of the shear viscosity with the composition for the mixture of CO_2 + *n*-decane at 311 K and 34 MPa. Comparison of the simulation results with the new AUA(4m) model and the previous simulations of Dysthe *et al.* [104] using the AUA3 with the experimental data of Cullik *et al.* [103].

5. Conclusion

The three fields in which we have cited recent applications of molecular simulation techniques raise difficult problems with classical thermodynamic approaches and justify thus to try molecular simulation as a possibly contributing technique.

In the first of these examples, related to the phase equilibria of H_2S–hydrocarbon mixtures, Gibbs ensemble Monte Carlo has allowed modelling of phase equilibria with an unprecedented extrapolation capability for pure components to mixtures. Although a specific interaction parameter was required to represent the H_2S–benzene system, the AUA potential of hydrocarbons has appeared well adapted to the prediction of systems involving H_2S and heavy hydrocarbons. Thanks to this potential, it has been possible to increase system size to investigate these systems sufficiently close to the critical point to allow a consistent determination of the critical coordinates. The reliability of critical point determinations can still be improved by the use of histogram reweighting methods coupled to finite size scaling [69]. Another perspective of improvement in this field is the explicit consideration of

the interface, so that new properties like the interfacial tension can be predicted [106–108] and the coupling of phase equilibria with reaction equilibria [109].

Beyond the other applications of H_2S–hydrocarbon phase equilibria [87], molecular simulation of phase equilibria has been applied to gas processing [23,27] natural gases [110] and it is also considered in several current projects. These comprise, among others, the phase equilibria of systems involving carbon dioxide (in the perspective of CO_2 reinjection in deep reservoirs), the behaviour of hydrogen in hydrocarbon processing and the thermodynamic properties of sulfur, nitrogen and oxygen-bearing compounds present in oil-derived or biomass-derived feedstocks.

The second application example, adsorption in zeolites, is probably much difficult from a scientific point of view because the oil industry is mostly interested in the behaviour of hydrocarbons (and pollutants) of low to moderate polarity, while the adsorbents considered are generally bearing electrostatic charges and cations and occasionally polar molecules like water. Thus it is less surprising that molecular simulation is just able to provide quantitative predictions of adsorption isotherms in selected cases and qualitative answers in most cases. Nevertheless, it is very encouraging that the introduction of a better physics through electrostatic and polarization energy contributions seems to improve significantly the predictions, either on pure component isotherms or on mixtures. The simulation of adsorption has already produced several relevant industrial applications like the trend of selectivities of branched alkanes in faujasites with different types of cations [23] and the influence of the silicon to aluminium ratio in sodium faujasites on the ortho/metaxylene selectivity [23], among other examples. However, the extension of these studies to other systems will still require significant efforts before reliable intermolecular potentials are available for a large range of zeolite structures and for other cations than sodium.

Transport properties, the third type of application quoted in this article, is a field where the intermolecular potentials developed for equilibrium properties of liquids allow already fair predictions in a large range of carbon number, pressure and temperature. As illustrated by the example of *n*-alkanes, the accuracy is however insufficient when using existing UA or AUA potentials and specific adaptations of these models are required to improve transport property predictions without changing significantly equilibrium properties. A comparable effort should now be made on other hydrocarbon families (aromatics, cyclic alkanes, nahthenoaromatics, olefins) in order to treat fuels and light oils in a realistic way. For aromatics, the OPLS All Atoms potential is known to provide excellent viscosity predictions for light isomers [58] but it would be delicate to extend this model to long chain alkylbenzenes, polyaromatics and naphthenoaromatics without spending excessive computing time. Also, a significant effort should be made to speed up calculations through parallelization and histogram reweighting [111], because it is difficult to compute viscosities larger than 10 MPa s with standard scalar computations. Non-equilibrium methods might provide more efficient ways of computation than the equilibrium MD considered in the present work, especially for thermal conductivity calculations [112].

It is likely that with all the possible improvements, transport property prediction from MD will be increasingly used in the oil and gas industry.

Acknowledgements

The authors thank total company for its support for some of the projects presented in this work. Jean-Marie Teuler (CNRS) is gratefully acknowledged for his contribution to the development and maintenance of molecular simulation software.

References

[1] R.L. Rowley, W.V. Wilding, J.L. Oscarson, N.A. Zundel, T.L. Marshall, T.E. Daubert, R.P. Danner. *DIPPR® Data Compilation of Pure Compound Properties*, Design Institute for Physical Properties, AIChE, New York (2002).
[2] J. Gmehling. *CODATA Bull.*, **58**, 56 (1985).
[3] D.Y. Peng, D.B. Robinson. *Ind. Chem. Eng. Fundam.*, **15**, 59 (1976).
[4] G. Soave. *Chem. Eng. Sci.*, **27**, 1197 (1972).
[5] G. Soave. *Ind. Eng. Chem. Res.*, **34**, 3981 (1995).
[6] B.I. Lee, M.G. Kesler. *AIChE J.*, **21**, 510 (1975).
[7] W.G. Chapman, K.E. Gubbins, G. Jackson, M. Radosz. *Fluid Phase Equilib.*, **52**, 31 (1989).
[8] L. Constantinou, R. Gani, J. O'Connell. *Fluid Phase Equilib.*, **103**, 11 (1995).
[9] H. Renon, J.M. Prausnitz. *Chem. Eng. Sci.*, **22**, 299 (1967).
[10] A. Fredenslund, J. Gmehling, P. Rasmussen. *Vapour–Liquid Equilibrium Using UNIFAC*, Elsevier, New York (1977).
[11] M.J. Huron, J. Vidal. *Fluid Phase Equilib.*, **1**, 247 (1979).
[12] D.M. Ruthven. *Principles of Adsorption and Adsorption Processes*, Wiley, New York (1984).
[13] A.L. Myers, J.M. Prausnitz. *AIChE J.*, **45**, 497 (1965).
[14] J. Lohrenz, B.G. Bray, C.R. Clark. *JPT*, **1964**, 1171 (1964).
[15] K.S. Pedersen, A. Fredenslund, P.L. Christiansen, P. Thomassen. *Chem. Eng. Sci.*, **39**, 1011 (1984).
[16] S.R.S. Sastri, K. Rao. *Chem. Eng. J.*, **50**, 9 (1992).
[17] M.J. Assael, J.P.M. Trusler, T.F. Tsolakis. *Thermophysical Properties of Fluids*, Imperial College Press, (1996).
[18] B.E. Poling, J.M. Prausnitz, J.P. O'Connell. *The Properties of Gases and Liquids*, 5th ed., McGraw Hill, New York (2001).
[19] J. Vidal. *Thermodynamique—Application au Génie Chimique et à l'Industrie Pétrolière*, Technip, Paris (1997).
[20] J.M. Prausnitz, R.N. Lichtenthaler, E.G.d. Azevedo. *Molecular Thermodynamics of Fluid-Phase Equilibria*, Prentice-Hall, Englewood Cliffs, NJ, USA (1986).
[21] M.P. Allen, D.J. Tildesley. *Computer Simulation of Liquids*, Oxford Science Publications, Oxford (1987).
[22] D. Frenkel, B. Smit. *Understanding Molecular Simulation*, Academic Press, San Diego (1996).
[23] P. Ungerer, P. Tavitian, A. Boutin. *Applications of Molecular Simulation in the Oil and Gas Industry—Monte Carlo Methods*, Editions Technip, Paris (2005).
[24] P. Ungerer, C. Nieto-Draghi, B. Rousseau, G. Ahunbay, V. Lachet. *J. Mol. Liq.*, (2007) accepted.
[25] J. Delhommelle, A. Boutin, A.H. Fuchs. *Mol. Simul.*, **22**, 351 (1999).
[26] J. Delhommelle, P. Millié, A.H. Fuchs. *Mol. Phys.*, **98**, 1895 (2000).

[27] P. Ungerer, A. Wender, G. Demoulin, E. Bourasseau, P. Mougin. *Mol. Simul.*, **30**, 631 (2004).
[28] A.Z. Panagiotopoulos. *Mol. Phys.*, **61**, 813 (1987).
[29] M. Mehta, D.A. Kofke. *Chem. Eng. Sci.*, **49**, 2633 (1994).
[30] R.Q. Snurr, A.T. Bell, D.N. Theodorou. *J. Phys. Chem.*, **97**, 13742 (1993).
[31] B. Smit. *Mol. Phys.*, **85**, 153 (1995).
[32] B. Smit. *J. Phys. Chem.*, **99**, 5597 (1995).
[33] D. Nicholson, N.G. Parsonage. *Computer Simulation and the Statistical Mechanics of Adsorption*, Academic Press, New York, USA (1982).
[34] M.D. Macedonia, E.J. Maginn. *Mol. Phys.*, **96**, 1375 (1999).
[35] T.J.H. Vlugt, R. Krishna, B. Smit. *J. Phys. Chem. B*, **103**, 1102 (1999).
[36] D. Dubbeldam, S. Calero, T.J.H. Vlugt, R. Krishna, T.L.M. Maesen, B. Smit. *J. Phys. Chem B*, **108**, 12301 (2004).
[37] M. Schenk, S. Calero, T.L.M. Maesen, T.J.H. Vlugt, L.L.v. Benthem, M.G. Verbeek, B. Schnell, B. Smit. *J. Catal.*, **214**, 88 (2003).
[38] P. Pascual, P. Pernot, P. Ungerer, B. Tavitian, A. Boutin. *Phys. Chem. Chem. Phys.*, **5**, 3684 (2003).
[39] P. Pascual, P. Ungerer, B. Tavitian, A. Boutin. *J. Phys. Chem. B*, **108**, 393 (2004).
[40] P. Pascual, A. Boutin, P. Ungerer, B. Tavitian, A.H. Fuchs. *Chem. Phys. Chem.*, **6**, 2015 (2004).
[41] V. Lachet, A. Boutin, B. Tavitian, A.H. Fuchs. *Langmuir*, **15**, 8678 (1999).
[42] V. Lachet, S. Buttefey, A. Boutin, A.H. Fuchs. *Phys. Chem. Chem. Phys.*, **3**, 80 (2001).
[43] C. Beauvais, X. Guerrault, F.-X. Coudert, A. Boutin, A.H. Fuchs. *J. Phys. Chem. B*, **108**, 399 (2004).
[44] C. Beauvais, A. Boutin, A.H. Fuchs. *Chem. Phys. Chem.*, 1 (2004).
[45] E. Jaramillo, S.M. Auerbach. *J. Phys. Chem. B*, **103**, 9589 (1999).
[46] S. Nosé. *J. Chem. Phys.*, **81**, 511 (1984).
[47] D.J. Evans, G.P. Morris. *Chem. Phys.*, **77**, 63 (1983).
[48] W.G. Hoover. *Phys. Rev. A*, **31**, 1695 (1985).
[49] J.P. Ryckaert, G. Ciccotti, H.J.C. Berendsen. *J. Comput. Phys.*, **23**, 327 (1977).
[50] J.P. Ryckaert, A. Bellemans. *Disc. Faraday Trans.*, **66**, 95 (1978).
[51] D. Dysthe, A.H. Fuchs, B. Rousseau. *J. Chem. Phys.*, **110**, 4047 (1999).
[52] D. Dysthe, A.H. Fuchs, B. Rousseau. *J. Chem. Phys.*, **112**, 7581 (2000).
[53] D. Dysthe, A.H. Fuchs, B. Rousseau. *J. Chem. Phys.*, **110**, 4060 (1999).
[54] W. Allen, R.L. Rowley. *J. Chem. Phys.*, **106**, 10273 (1997).
[55] L.I. Kioupis, Maginn. *J. Phys. Chem. B*, **103**, 10781 (1999).
[56] L.I. Kioupis, E.J. Maginn. *J. Phys. Chem. B*, **104**, 7774 (2000).
[57] R.L. Rowley, J.F. Ely. *Mol. Phys.*, **75**, 713 (1992).
[58] B. Rousseau, J. Petravic. *J. Phys. Chem. B*, **106**, 13010 (2002).
[59] B. Smit, S. Karaborni, J.I. Siepmann. *J. Chem. Phys.*, **102**, 2126 (1995).
[60] J.R. Errington, A.Z. Panagiotopoulos. *J. Chem. Phys.*, **111**, 9731 (1999).
[61] E. Bourasseau, P. Ungerer, A. Boutin. *J. Phys. Chem. B*, **106**, 5483 (2002).
[62] E. Bourasseau, P. Ungerer, A. Boutin, A.H. Fuchs. *Mol. Simul.*, **28**, 317 (2002).
[63] L.R. Dodd, T.D. Boone, D.N. Theodorou. *Mol. Phys.*, **78**, 961 (1993).
[64] N. Wilding. *Phys. Rev. E*, **53**, 926 (1995).
[65] J.L. Barrat, J.P. Hansen. *Basic Concepts for Simple and Complex Liquids*, Cambridge University Press, Cambridge, UK (2003).
[66] J.J.-C. Hsu, N. Nagarajan, R.L. Robinson. *J. Chem. Eng. Data*, **30**, 485 (1985).
[67] J.C. Rainwater, F.R. Williamson. *Int. J. Thermophys.*, **7**, 65 (1986).
[68] M.R. Moldover, J.C. Rainwater. *J. Chem. Phys.*, **88**, 7772 (1988).
[69] J.J. Potoff, A.Z. Panagiotopoulos. *J. Chem. Phys.*, **109**, 10914 (1998).
[70] S. Nath. *J. Phys. Chem. B*, **107**, 9498 (2003).
[71] G. Kamath, Lubna, J.J. Potoff. *J. Chem. Phys.*, **123**, 124505 (2005).
[72] T. Kristof, J. Liszi. *J. Phys. Chem. B*, **101**, 5480 (1997).
[73] J. Vorholz, B. Rumpf, G. Maurer. *Phys. Chem. Chem. Phys.*, **4**, 4449 (2002).
[74] C. Nieto-Draghi, A.D. Mackie, J. Bonet-Avalos. *J. Chem. Phys.*, **123**, 014505 (2005).
[75] O. Contreras-Camacho, V. Lachet, M.G. Ahunbay, J. Perez, P. Ungerer, A. Boutin, A.D. Mackie. *J. Phys. Chem. B*, **108**, 14115 (2004).
[76] M.G. Ahunbay, J. Perez-Pellitero, R.O. Contreras-Camacho, J.M. Teuler, P. Ungerer, A.D. Mackie, V. Lachet. *J. Phys. Chem. B*, **109**, 2970 (2005).
[77] O. Contreras-Camacho, P. Ungerer, A. Boutin, A.D. Mackie. *J. Phys. Chem. B*, **108**, 14109 (2004).
[78] P. Ungerer, C. Beauvais, J. Delhommelle, A. Boutin, B. Rousseau, A.H. Fuchs. *J. Chem. Phys.*, **112**, 5499 (2000).
[79] W.L. Jorgensen, D.L. Severance. *J. Am. Chem. Soc.*, **112**, 4768 (1990).
[80] W.L. Jorgensen, E.R. Laird, T.B. Nguyen, J. Tirado-Rives. *J. Comput. Chem.*, **14**, 206 (1993).
[81] W.L. Jorgensen, T.B. Nguyen. *J. Comput. Chem.*, **14**, 195 (1993).
[82] M. Neumann. *J. Chem. Phys.*, **82**, 5663 (1985).
[83] M. Neumann. *J. Chem. Phys.*, **1567** (1986).
[84] S. Laugier, D. Richon. *J. Chem. Eng. Data*, **40**, 153 (1995).
[85] H.H. Reamer, B.H. Sage, W.N. Lacey. *Ind. Eng. Chem.*, **45**, 1805 (1953).
[86] G. Feng, A.E. Mather. *J. Chem. Eng. Data*, **37**, 412 (1992).
[87] P. Ungerer, V. Lachet, B. Tavitian. *Oil Gas Sci. Technol.*, **61**, 387 (2006).
[88] J.G. Harris, K.H. Yung. *J. Phys. Chem.*, **99**, 12021 (1995).
[89] W.L. Jorgensen, J. Chandrasekhar, J.D. Madura. *J. Chem. Phys.*, **79**, 926 (1983).
[90] J. Delhommelle, C. Tschirwitz, P. Ungerer, G. Granucci, P. Millié, D. Pattou, A.H. Fuchs. *J. Phys. Chem. B*, **104**, 4745 (2000).
[91] J.L. Lievens, W.J. Mortier, J.P. Verduijn. *J. Phys. Chem.*, **96**, 5473 (1992).
[92] W.J. Mortier, S.K. Ghosh, S. Shankar. *J. Am. Chem. Soc.*, **108**, 4315 (1986).
[93] J.J.d. Pablo, M. Laso, U.W. Suter. *J. Chem. Phys.*, **96**, 6157 (1992).
[94] R. Faller, Q. Yan, J.J. dePablo. *J. Chem. Phys.*, **116**, 5419 (2002).
[95] S. Calero, D. Dubbeldam, R. Krishna, B. Smit, T.J.H. Vlugt, J.F.M. Denayer, J.A. Martens, T.L.M. Maesen. *J. Am. Chem. Soc.*, **126**, 11377 (2004).
[96] A.d. Lella, N. Desbiens, A. Boutin, I. Demachy, P. Ungerer, J.P. Bellat, A.H. Fuchs. *Phys. Chem. Chem. Phys.*, **8**, 5396 (2006).
[97] P.E. Smith, W.F.v. Gunsteren. *Chem. Phys. Lett.*, **215**, 315 (1993).
[98] M. Mondello, G.S. Grest. *J. Chem. Phys.*, **106**, 9327 (1997).
[99] H. Zhang, F.F. Ely. *Fluid Phase Equilib.*, **217**, 111 (2004).
[100] C. McCabe, C.W. Manke, P.T. Cummings. *J. Chem. Phys.*, **116**, 3339 (2002).
[101] C. Nieto-Draghi, P. Ungerer, B. Rousseau. *J. Chem. Phys.*, **125**, 044517 (2006).
[102] K. Travis, D. Brown, J.H.R. Clarke. *J. Chem. Phys.*, **102**, 2174 (1995).
[103] A.S. Cullick, M. Mathis. *J. Chem. Eng. Data*, **29**, 393 (1984).
[104] D.K. Dysthe, A.H. Fuchs, B. Rousseau. *Int. J. Thermophys.*, **19**, 437 (1998).
[105] P. Padilla, S. Toxvaerd. *J. Chem. Phys.*, **94**, 5650 (1991).
[106] F. Goujon, P. Malfreyt. *J. Chem. Phys.*, **116**, 8106 (2002).
[107] B. Chen, J.I. Siepmann, M.L. Klein. *J. Am. Chem. Soc.*, **124**, 12232 (2002).
[108] G.J. Gloor, G. Jackson, F.J. Blas, E.d. Miguel. *J. Chem. Phys.*, **123**, 134703 (2005).
[109] M. Lisal, W.R. Smith, I. Nezbeda. *AIChE J.*, **46**, 4 (2000).
[110] F. Escobedo. *J. Chem. Phys.*, **110**, 11999 (1999).
[111] C. Nieto-Draghi, J. Perez-Pellitero, Bonet-Avalos. *J. Phys. Rev. Lett.*, **95**, 040603 (2005).
[112] F. Müller-Plathe, D. Reith. *Comput. Theor. Polym. Sci.*, **9**, 203 (1999).
[113] M.S. Sun, O. Talu, D.B. Shah. *J. Phys. Chem.*, **100**, 17276 (1996).
[114] A. Wender, A. Barreau, C. Lefebvre, A.D. Lella, A. Boutin, P. Ungerer, A.H. Fuchs. *Adsorp. Sci. Technol.*, (2007) accepted.
[115] J.F.M. Denayer, G.V. Baron. *Adsorption*, **3**, 251 (1997).
[116] J.C. Moïse, J.P. Bellat, A. Méthivier. *Micropor. Mesopor. Mater.*, **43**, 91 (2001).
[117] K.R. Harris, R. Malhortra, L.A. Woolf. *J. Chem. Eng. Data*, **42**, 1254 (1997).
[118] D.R. Caudwell, J.P.M. Trusler, W.A. Wakeham. *Int. J. Thermophys.*, **25**, 1339 (2004).